

# Operator-Consistent Physics-Informed Learning for Wafer Thermal Reconstruction in Lithography

Ze Tao<sup>1</sup>, Yuxi Jin<sup>1</sup>, Ke Xu<sup>1</sup>, Haoran Xu<sup>1</sup>, Hanxuan Wang<sup>2</sup>,  
Fujun Liu<sup>1\*</sup>

<sup>1</sup>\*Nanophotonics and Biophotonics Key Laboratory of Jilin Province,  
School of Physics, Changchun University of Science and Technology,  
Changchun, 130022, P.R. China.

<sup>2</sup>Faculty of Chinese Medicine, Macau University of Science and  
Technology, Macau, 999078, P.R. China.

\*Corresponding author(s). E-mail(s): [fjliu@cust.edu.cn](mailto:fjliu@cust.edu.cn);

## Abstract

Thermal field reconstruction in post-exposure bake (PEB) is critical for advanced lithography, but current methods lack consistent accuracy and physical alignment. To bridge this gap, we introduce a physics-informed neural model that unifies coordinates, fields, and differential operators on a single computation graph using gated liquid layers. Applied to a 2D PEB scenario with internal heat generation and convective boundaries, the model formulates residuals via differential forms and a loss functional integrating closure, balance, and trace misfits. The results demonstrate rapid convergence, uniformly low errors, and strong agreement with FEM benchmarks, achieving stable training without oscillation. Our framework outperforms existing baselines in accuracy and robustness, establishing a reliable foundation for high-fidelity thermal modeling and offering a transferable strategy for operator-consistent neural surrogates in other physical domains.

**Keywords:** Liquid Neural Networks, Long Short-Term Memory, Physics-Informed Neural Networks, Operator Alignment

## 1 Introduction

The post-exposure bake (PEB) stage is a decisive factor in photolithographic processing, directly determining critical dimension control and line-edge roughness across semiconductor wafers. Precise thermal management during this phase impacts the fidelity of pattern transfer, yield, and device reliability in advanced integrated circuits [1–4]. As wafer size and power density continue to scale, conventional heat dissipation strategies face increasing limitations in capturing non-uniform temperature distributions and geometry-sensitive flux patterns [5]. These limitations are particularly evident when high-resolution reconstructions are required across large-scale substrates with spatially heterogeneous boundary conditions [6–9]. Consequently, developing a thermal reconstruction framework that incorporates physical constraints while adapting to the complex geometry–port coupling inherent to wafer-scale conduction is essential for reliable process control and accurate inverse design [10–15].

Prior research has established various physics-informed modeling strategies that integrate physical laws into neural approximators [11, 16–23, 23–31]. These methods can match governing equations, enforce boundary conditions, and achieve reasonable generalization across many heat transfer scenarios [16, 32–38, 38–49]. However, most existing frameworks lack a consistent alignment between geometric coordinates, physical fields, and differential operators [18, 50–59]. This fundamental mismatch often leads to a failure in regulating operator-level conditioning and reshaping internal representations in response to local spectral variations [60–64], ultimately resulting in degraded accuracy near critical regions and limiting the ability to construct uniformly reliable surrogates for high-precision thermal reconstruction [65–67].

Recent developments in hybrid neural architectures offer a promising path toward resolving these limitations [68, 69]. Operator-aligned designs that incorporate gated dynamics, for instance, can regulate spectral behavior, stabilize higher-order derivatives, and preserve the structure of physical laws across computation graphs. By embedding single-step gating within a liquid neural backbone, it becomes possible to dynamically control local conditioning while maintaining a unified pipeline from coordinates to fields to operators. This configuration not only retains the benefits of physical supervision but also adapts the predictor’s response to the intrinsic structure of the solution space, thereby establishing a consistent representation across layers and scales that is well-suited for high-fidelity thermal field reconstructions under process-driven constraints.

We deploy this hybrid architecture on the PEB heat-flux reconstruction task and achieve high-fidelity results across all evaluation metrics. The predicted temperature field closely matches the benchmark solution, with uniformly low absolute errors maintained throughout the entire domain. Furthermore, residual losses in both governing equations and boundary conditions exhibit synchronized decay and settle into stable plateaus without late-stage fluctuations. These outcomes confirm that the model maintains operator-level consistency and geometric coherence during training, establishing a reliable foundation for wafer-scale thermal reconstruction under process-aligned constraints and marking a substantial advancement in physics-informed heat transfer modeling.

## 2 Operator-Aligned Network under Geometry–Port Consistency

This study proposes and implements a Physics-Informed Neural Network architecture based on Liquid Neural Networks (LNN) to solve two-dimensional PEB process heat transfer problems with internal heat generation and convective boundary conditions. As illustrated in Fig. 1 (a), this architecture replaces conventional MLPs with a dynamically evolving network that incorporates state differential equations and adaptive neuron coupling to enhance the joint modeling of local responses and global physical patterns. The predictor is treated as a typed operator map  $\Phi_\theta : \Omega \rightarrow H^1(\Omega)$ , enabling the computation graph to simultaneously yield  $\nabla T_\theta$  and  $\nabla^2 T_\theta$  through automatic differentiation, thereby directly evaluating interior and boundary differential quantities along with required trace mappings.

The second derivatives of the network map are controlled through the Supplementary Information (SI) "sum–product" inequality (Eq. (S89)), which couples layerwise second-order constant  $H_\ell$  with first-order constant  $L_j$

$$\|D^2\Phi_\theta\|_{\text{op}} \leq \sum_{\ell=1}^m \left( H_\ell \prod_{j=\ell+1}^m L_j^2 \prod_{j=1}^{\ell-1} L_j \right), \quad L_j := \sup_z \|DF_j(z)\|_{\text{op}}, \quad H_j := \sup_z \|D^2F_j(z)\|_{\text{op}}. \quad (1)$$

A tighter bound for a single gated layer is provided by Eq. (S88)

$$\|D^2\Phi_\theta\|_{\text{op}} \leq \beta_g \|W\|^2 \|W^{(\text{out})}\|^2, \quad (2)$$

with transfer to physical second-order operators following from Eq. (S41), yielding  $\|\nabla^2 T_\theta\|_{\text{op}} \leq C_{\text{geom}} \|D^2\Phi_\theta\|_{\text{op}}$ . The network adopts a "single-gating, single-readout" feedforward execution without time unrolling, where gate variables  $(i, f, o)$  modify only the local condition number and spectral shape of  $\Phi_\theta$  without altering the covariant relations between geometry and operators. Proofs of "preconditioned residual equivalence" and "product-type upper bound for the second derivative" are provided in the Sec. I of the Supplementary Information (SI), while the main text maintains focus on alignment between function-space types and operator channels.

Spatial coordinates  $\mathbf{x} = (x, y) \in \Omega \subset \mathbb{R}^2$  serve as network inputs, projected to the first LNN layer containing  $d = 64$  liquid neurons. Each neuron receives combined current input and historical states, updates its internal state, and propagates outputs to subsequent layers. The internal state  $\mathbf{h}_i(t) \in \mathbb{R}$  of each liquid neuron follows a continuous-time dynamic system

$$\frac{d\mathbf{h}_i(t)}{dt} = -\lambda_i \mathbf{h}_i(t) + \phi_i(\mathbf{x}, \mathbf{h}_i(t); \theta_i) \quad (3)$$

where  $\lambda_i > 0$  denotes the leak coefficient and  $\phi_i$  represents a nonlinear response function determined by neuron coupling, input projection, and bias. For numerical

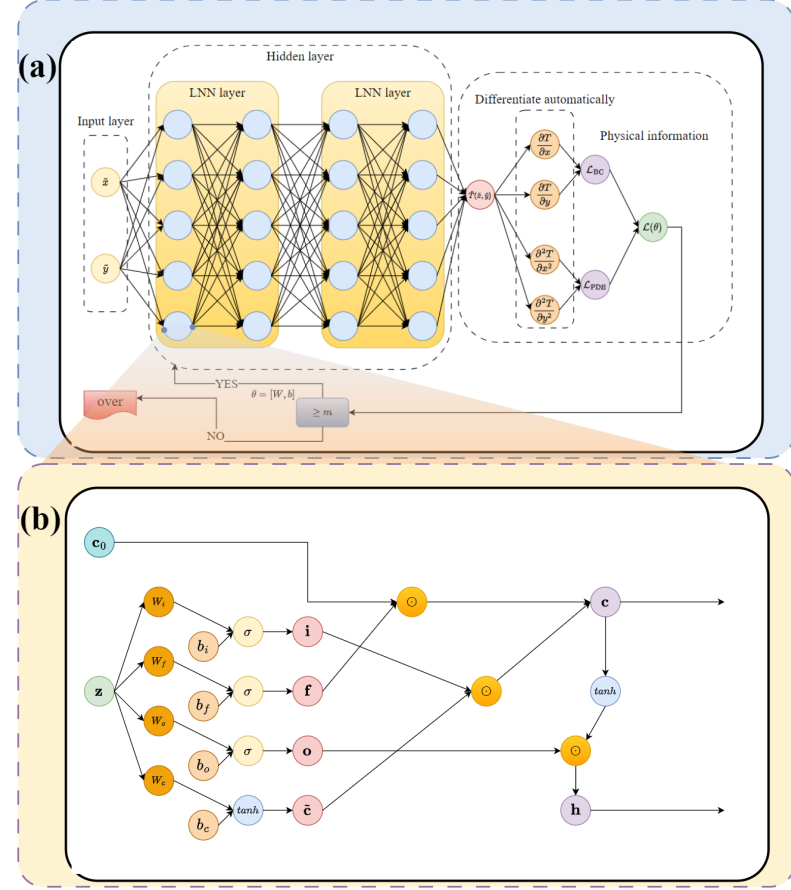


**Fig. 1:** We present an LSTM-gated LNN-PINN architecture that maps spatial coordinates to temperature via a shared trunk and branches into physics heads for PDE, boundary/port, and source residuals. Residual channels aggregate into a single energy-consistent loss, stabilizing training and delivering high-fidelity predictions with accurate boundary traces. **(a)** Structure of the Physics-Informed Neural Network (LSTM-LNN-PINN) incorporating Gated Liquid Neural Networks. The original Multi-Layer Perceptron (MLP) is replaced by Liquid Neural Network (LNN) modules with Long Short-Term Memory (LSTM) gating mechanisms, forming a two-layer gated LNN network with 64 neurons per layer. This design dynamically adjusts information flow and feature extraction capabilities, enhancing modeling performance for spatiotemporal nonlinear behaviors in complex PEB process heat transfer fields while preserving physical constraints. The figure illustrates the interconnections and data flow among submodules, reflecting the deep integration of physical knowledge with neural network innovations. **(b)** Computation diagram of a Long Short-Term Memory (LSTM) unit, showing the input gate, forget gate, output gate, and candidate cell state. The figure illustrates affine transformations of weights and biases, nonlinear activation mappings, element-wise gate multiplications, weighted updates of previous cell state  $\mathbf{c}_0$ , generation of current cell state  $\mathbf{c}$ , and final hidden state  $\mathbf{h}$  modulated by tanh and output gate. This demonstrates the memory retention and selective forgetting mechanisms inherent to Long Short-Term Memory (LSTM) units for sequence modeling in PEB process heat transfer fields.

implementation, explicit Euler integration provides one-step approximation

$$\mathbf{h}_i \approx \alpha_i \mathbf{h}_i^{(0)} + (1 - \alpha_i) \phi_i \left( \mathbf{x}, \mathbf{h}_i^{(0)} \right), \quad \alpha_i = e^{-\lambda_i \Delta t} \quad (4)$$

where  $\Delta t = 1$  is absorbed into the network weights by default. This mechanism enables neurons to respond to external inputs while maintaining internal coupling, explicitly capturing the competition between exponential state decay and input-driven updates. The internal function  $\phi_i$  adopts a linear form

$$\phi_i(\mathbf{x}, \mathbf{h}) = \sigma \left( \sum_{j=1}^d W_{ij}^{(\text{recur})} h_j + \sum_{k=1}^2 W_{ik}^{(\text{in})} x_k + b_i \right) \quad (5)$$

where  $W^{(\text{in})} \in \mathbb{R}^{d \times 2}$  projects spatial coordinates to neurons, and  $W^{(\text{recur})} \in \mathbb{R}^{d \times d}$  is a learnable recurrent matrix controlling state propagation. The input vector  $\mathbf{x} = (x, y)^T$  undergoes linear transformation by  $W^{(\text{in})}$ , combines with neuron states, and passes through nonlinear activation to produce final responses.

Gating mechanisms are employed at all layers for state propagation and memory control, as illustrated in Fig. 1 (b), following a structure similar to conventional Long Short-Term Memory (LSTM) networks. At each layer, gating vectors  $\mathbf{i}, \mathbf{f}, \mathbf{o} \in \mathbb{R}^d$  represent the input gate, forget gate, and output gate, updated through the equations

$$\begin{aligned} \mathbf{i} &= \sigma(W_i \mathbf{z} + b_i) \\ \mathbf{f} &= \sigma(W_f \mathbf{z} + b_f) \\ \mathbf{o} &= \sigma(W_o \mathbf{z} + b_o) \\ \tilde{\mathbf{c}} &= \tanh(W_c \mathbf{z} + b_c) \end{aligned} \quad (6)$$

where  $\mathbf{z} = [\mathbf{x}; \mathbf{h}_0] \in \mathbb{R}^{d+2}$  concatenates the current input and previous hidden state  $\mathbf{h}_0$ .  $W_{i,f,o,c}$  are weight matrices controlling input writing, memory forgetting, hidden output, and candidate memory generation, respectively;  $b_{i,f,o,c}$  are bias vectors. The state updates follow

$$\begin{aligned} \mathbf{c} &= \mathbf{f} \odot \mathbf{c}_0 + \mathbf{i} \odot \tilde{\mathbf{c}} \\ \mathbf{h} &= \mathbf{o} \odot \tanh(\mathbf{c}) \end{aligned} \quad (7)$$

with  $\odot$  denoting element-wise multiplication,  $\mathbf{c}_0$  the previous cell state,  $\mathbf{c}$  the updated cell state, and  $\mathbf{h}$  the current hidden state. This gating structure enables selective memory, forgetting, and output of local spatial perturbations, thereby enhancing local generalization capabilities in PEB process heat transfer modeling.

Several key distinctions differentiate our approach from existing architectures. Compared to static MLP-PINN, we place pointwise gating  $(i, f, o)$  in every layer to induce an input-dependent diagonal preconditioner  $D_{i,f,o}(x)$ , ensuring the linearization satisfies  $J(x) = D_{i,f,o}(x)W + S(x)$  with  $S$  bounded and skew-symmetric. This allows inputs to adaptively reshape local spectra and control the amplification factor of  $\nabla^2 T_\theta$ , a property not available in the layerwise Jacobian of standard MLPs. Relative to LNN-PINN with leaky single gates, we decouple "leak/injection/readout" into

three distinct gates ( $f, i, o$ ), emphasizing "contraction-step size-readout" in the main text. A small-gain argument pushes the spectral radius of the hidden-to-hidden map into a controllable interval  $\rho < 1$ , thereby stabilizing second-order operator evaluation. In contrast to LSTM-PINN with explicit sequence axes, we retain the conditioning benefits of gating while removing time unrolling: single-step gating achieves first-order accuracy equivalent to a residual block with input-dependent diagonal preconditioning, maintaining computational complexity comparable to a same-width fully connected layer while avoiding extra backpropagation depth.

We aggregate the typed residual channels on the same computation graph using the loss definition from Eq. (S151) of the Supplementary Information (SI).

$$\begin{aligned} \mathcal{L}(T_\theta) = & w_1^2 \int_{\Omega} \langle K^{-1} \mathcal{R}_{\text{twist}}, \mathcal{R}_{\text{twist}} \rangle dV_g + w_2^2 \int_{\Omega} h_\Omega^2 |\mathcal{R}_{\text{div}}|^2 dV_g \\ & + w_3^2 \int_{\Omega} \langle K \mathcal{R}_{\text{cl}}, \mathcal{R}_{\text{cl}} \rangle dV_g + w_4^2 \int_{\partial\Omega} h_\Gamma |\mathcal{R}_{\text{port}}|^2 dS_g, \end{aligned} \quad (8)$$

where  $\mathcal{R}_{\text{twist}} = K \nabla e$ ,  $\mathcal{R}_{\text{div}} = \nabla \cdot (K \nabla e)$ ,  $\mathcal{R}_{\text{port}} = n \cdot K \nabla e + h \gamma_0 e$  as defined in Eqs. (S146)-(S151) of the Supplementary Information (SI). Invoking the two-sided equivalence from the Eqs. (S148), (S161) and (S162) of the Supplementary Information (SI) aligns the training objective with the energy error

$$c_{\text{low}} \|e\|_E^2 \leq \mathcal{L}(T_\theta) \leq c_{\text{up}} \|e\|_E^2 \quad (\text{osc} = 0), \quad (9)$$

with constants depending only on  $(k_0, \|K\|_\infty, h_0, \|h\|_\infty)$  and geometric regularity of  $\Omega$ . The rigorous relations among these three components and all constant dependencies are detailed in the Sec. II of the Supplementary Information (SI).

The complete set of learnable parameters is defined as

$$\theta = \left\{ W^{(\text{in})}, b^{(\text{in})}, W_i, U_i, b_i, W_f, U_f, b_f, W_o, U_o, b_o, W_c, U_c, b_c, W^{(\text{recur})}, \lambda, W^{(\text{out})}, b^{(\text{out})} \right\} \quad (10)$$

In implementation, `model.parameters()` automatically collects this set for backpropagation.

The training objective minimizes the sum of the predicted temperature field and PDE residuals using the Adam optimizer. At step  $t$ , first- and second-moment estimates update parameters through

$$\begin{aligned} \mathbf{m}_t &= \beta_1 \mathbf{m}_{t-1} + (1 - \beta_1) \nabla_\theta \mathcal{L}_t \\ \mathbf{v}_t &= \beta_2 \mathbf{v}_{t-1} + (1 - \beta_2) (\nabla_\theta \mathcal{L}_t)^2 \\ \hat{\mathbf{m}}_t &= \frac{\mathbf{m}_t}{1 - \beta_1^t}, \quad \hat{\mathbf{v}}_t = \frac{\mathbf{v}_t}{1 - \beta_2^t} \\ \boldsymbol{\theta}_{t+1} &= \boldsymbol{\theta}_t - \eta \cdot \frac{\hat{\mathbf{m}}_t}{\sqrt{\hat{\mathbf{v}}_t} + \epsilon} \end{aligned} \quad (11)$$

with default values  $\beta_1 = 0.9$ ,  $\beta_2 = 0.999$ ,  $\epsilon = 10^{-8}$ , and learning rate  $\eta$ . Gradients  $\nabla_\theta \mathcal{L}_t$  are computed for the total loss  $\mathcal{L}_t$  at step  $t$ . We employ a fixed learning rate and

train the model for 50,000 iterations to ensure both data fitting at observation points and adherence to physical constraints under non-explicit boundary conditions. This iteration count exceeds the plateau point of operator residual-energy trajectories across all backbones, matches the normalization in Tab. 1 (time/epoch = total/50,000), and ensures a uniform computational budget for cross-model RMSE comparisons.

The overall architecture implements "coordinates  $\rightarrow$  fields  $\rightarrow$  operator/trace" as a single computational chain, where the mixed backbone provides provable conditioning control within the network without altering the geometry–port–operator pipeline or the symbol system. The Sec. III of the Supplementary Information (SI) records three theorems corresponding to this section: preconditioning equivalence, non-expansiveness with a second-order upper bound, and affine covariance.

### 3 Geometric–Port Formulation for PEB Heat-Flux and Objective Construction

Let us focus on the heat-flux pathway during the post-exposure bake (PEB) stage of lithographic processing, where the wafer behaves as a two-dimensional conductive plate governed by an isotropic law  $K(x) = k, \text{Id}$  with Robin (convection) boundary conditions at ambient temperature  $T_\infty$ . We consider a circular domain with radius  $R = 150$  mm and employ the following physical constants in Eqs. (13)–(18):  $k = 159 \text{ W, m}^{-1}\text{K}^{-1}$ ,  $Q = 2000 \text{ W, m}^{-3}$ ,  $h = 50 \text{ W, m}^{-2}\text{K}^{-1}$ , and  $T_\infty = 800 \text{ K}$ . The mathematical framework operates on an oriented Riemannian manifold with boundary  $(\Omega, g)$  and outward unit normal  $n$ , where the Hodge star induced by  $g$  is denoted by  $*$  (with the subscript  $g$  omitted hereafter). Temperature  $T \in H^1(\Omega)$  is treated as a 0-form, flux covector  $\iota = q^\flat \in \Lambda^1(\Omega)$  as a 1-form, and the  $K$ -twist  $\omega := K^{-1}\iota \in \Lambda^1(\Omega)$ . We utilize the exterior derivative  $d$ , codifferential  $\delta := -*d*$ , trace operators  $\gamma_0 : H^1(\Omega) \rightarrow H^{1/2}(\partial\Omega)$  and  $\gamma_n : H(\text{div}; \Omega) \rightarrow H^{-1/2}(\partial\Omega)$ , and set  $\lambda := \gamma_0 T$ . With the bundle connection  $A \equiv 0$  ensuring  $d_A = d$  and  $F_A = 0$ , we collect state and port variables into

$$U := (\omega, \iota, T, \lambda), \quad (12)$$

where  $T \in H^1(\Omega)$  is the temperature potential (a 0-form),  $\omega \in L^2\Lambda^1(\Omega)$  is the  $K$ -twist 1-form,  $\iota \in H(\text{div}; \Omega)$  is the heat-flux covector with well-defined normal trace  $\gamma_n \iota \in H^{-1/2}(\partial\Omega)$ , and  $\lambda := \gamma_0 T \in H^{1/2}(\partial\Omega)$  is the Dirichlet trace. We denote by  $d$  the exterior derivative, by  $\delta := -*d*$  the codifferential, and by  $\nabla T := dT$  the metric gradient 1-form. The material tensor  $K(x)$  is symmetric positive definite with lower bound  $k_0 > 0$ , and the port impedance  $h(x) \geq h_0 > 0$ . Using this notation, we assemble the constitutive-operator system in block form

$$\mathbb{A} U = \begin{bmatrix} d & 0 & 0 & 0 \\ 0 & \delta & 0 & 0 \\ I & 0 & \nabla & 0 \\ 0 & \gamma_n & 0 & -h \\ 0 & 0 & -\gamma_0 & I \end{bmatrix} \begin{bmatrix} \omega \\ \iota \\ T \\ \lambda \end{bmatrix} = \begin{bmatrix} 0 \\ Q \text{vol}_g \\ 0 \\ h T_\infty \\ 0 \end{bmatrix}. \quad (13)$$

Componentwise, this system expands to

$$d\omega = 0 \text{ in } \Omega, \quad \delta\iota = Q \text{ vol}_g \text{ in } \Omega, \quad \iota(n) = h(\lambda - T_\infty) \text{ on } \partial\Omega, \quad \omega + \nabla T = 0 \text{ in } \Omega, \quad \lambda = \gamma_0 T. \quad (14)$$

Using the same notation, we define the  $K$ -twist residual vector  $\mathcal{R}(U) := \mathbb{A}U - (0, Q \text{ vol}_g, 0, hT_\infty, 0)^\top$  with entries

$$\mathcal{R} = \begin{bmatrix} \mathcal{R}_{\text{clo}} \\ \mathcal{R}_{\text{div}} \\ \mathcal{R}_{\text{twist}} \\ \mathcal{R}_{\text{port}} \\ \lambda - \gamma_0 T \end{bmatrix} = \begin{bmatrix} d\omega \\ \delta\iota - Q \text{ vol}_g \\ \omega + \nabla T \\ \iota(n) - h(\lambda - T_\infty) \\ 0 \end{bmatrix}, \quad (15)$$

measuring all interior terms by the Hodge inner product induced by  $g$ . This approach maintains consistent units (energy-density integrated over volume or boundary) and aligns operator blocks with the weak formulation used subsequently, with detailed proofs and constants provided in the Sec. IV of the Supplementary Information (SI).

We define the PDE and boundary losses as

$$\mathcal{L}_{\text{PDE}} = w_1 \int_{\Omega} \mathcal{R}_{\text{twist}} \wedge * \mathcal{R}_{\text{twist}} + w_2 \int_{\Omega} \mathcal{R}_{\text{div}} \wedge * \mathcal{R}_{\text{div}} + w_3 \int_{\Omega} \mathcal{R}_{\text{clo}} \wedge * \mathcal{R}_{\text{clo}}, \quad (16)$$

$$\mathcal{L}_{\text{BC}} = w_4 \int_{\partial\Omega} |\mathcal{R}_{\text{port}}|^2 \, ds, \quad (17)$$

and take the objective as the sum

$$\mathcal{L} = \mathcal{L}_{\text{PDE}} + \mathcal{L}_{\text{BC}}. \quad (18)$$

Weights  $(w_1, \dots, w_4)$  follow non-dimensional scaling described below, where coercivity of the induced energy norm and the two-sided equivalence between  $\mathcal{L}$  and the weak energy error depend only on  $(k_0, |K|_\infty, h_0, |h|_\infty)$  and geometric regularity of  $\Omega$ , with complete statements and proofs in the Sec. V of the Supplementary Information (SI).

Non-dimensionalization employs scaled coordinates with  $x' = x/L$ ,  $T' = T/(Q_0 L^2/k_0)$ ,  $K' = K/k_0$ ,  $h' = hL/k_0$ ,  $Q' = Q/Q_0$ . After rewriting all integrals in the  $(x', \cdot)$  frame, we set

$$w_1 \simeq 1, \quad w_2 \simeq \|K'\|_\infty^{-1}, \quad w_3 \simeq \varepsilon_{\text{clo}}, \quad w_4 \simeq 1, \quad (19)$$

using  $\varepsilon_{\text{clo}}$  to suppress the deviation of  $\omega$  relative to  $-\nabla T$ , matching the port penalty with the volumetric terms in order, and concentrating anisotropy strength in  $\|K'\|_\infty$ . The two-sided constants depend only on  $(k_0, \|K\|_\infty, h_0, \|h\|_\infty)$  and domain geometry; we place the full proof in the Sec. VI of the Supplementary Information (SI).

To establish verifiable local energy relations, we define the absolute error map and pointwise alignment of the three residuals. Letting  $T^*$  denote the true solution,  $e := T - T^*$  the error, and the energy norm  $\|e\|_E^2 = \int_{\Omega} \langle K \nabla e, \nabla e \rangle + \int_{\partial\Omega} h(\gamma_0 e)^2$ .

Take a smooth partition of unity  $\{\phi_i\}$  covering  $\Omega$ , each  $\phi_i$  supported in a micro-patch  $\omega_i$  of diameter  $\simeq h_i$ , and set  $\Gamma_i := \partial\Omega \cap \omega_i$ . Under Robin boundary and coercivity assumptions, define the local indicator

$$\eta_i^2 := \alpha_1 \int_{\omega_i} \|\mathcal{R}_{\text{twist}}\|^2 + \alpha_2 h_i^2 \int_{\omega_i} \|\mathcal{R}_{\text{div}}\|^2 + \alpha_3 h_i \int_{\Gamma_i} |\mathcal{R}_{\text{port}}|^2, \quad (20)$$

where  $\alpha_{1,2,3}$  depend only on  $(k_0, \|K\|_\infty, h_0, \|h\|_\infty)$  and shape regularity. In the Sec. VII of the Supplementary Information (SI) we prove the two-sided estimate

$$c_1 \sum_i \eta_i^2 \leq \|e\|_E^2 \leq c_2 \sum_i \eta_i^2, \quad (21)$$

and we provide the “local reliability/effectivity” version

$$c'_1 \eta_i^2 \leq \int_{\omega_i} \langle K \nabla e, \nabla e \rangle + \int_{\Gamma_i} h(\gamma_0 e)^2 \leq c'_2 \eta_i^2. \quad (22)$$

These bounds establish a one-to-one correspondence between spatial distribution of error-energy density and local densities of  $|\mathcal{R}_{\text{twist}}|^2$ ,  $h_i^2 |\mathcal{R}_{\text{div}}|^2$ , and  $h_i |\mathcal{R}_{\text{port}}|^2$ . Within any  $\omega_i$ , the peaks and valleys of error maps  $|e|$  and  $|\nabla e|$  align with those of  $\eta_i$  within constant factors and the local smoothing-kernel scale  $h_i$ , providing precise meaning to “pointwise alignment.” Physically, the volumetric equation residual  $\mathcal{R}_{\text{div}}$  releases  $h_i$ -scale energy inside  $\omega_i$  via the Green kernel, the port residual  $\mathcal{R}_{\text{port}}$  conducts inward along  $\Gamma_i$  forming boundary-layer error ridges, and the constitutive residual  $\mathcal{R}_{\text{twist}}$  enforces consistency between  $\nabla T$  and flux, thereby locking error peaks to geometric locations with strongest gradient mismatch. The Sec. VIII of the Supplementary Information (SI) provides precise lemmas localizing the  $H^{-1}/H^{-1/2}$  terms to  $\omega_i$  through partition-of-unity lifting, Bogovskii operator, and stable extension, while explaining why smooth network predictors admit negligible interior jump terms that yield the scalings  $h_i^2$  and  $h_i$ .

For quantitative validation, we employ a MATLAB finite-element solution as a noise-free reference field, computing two key metrics at identical sample points: the root mean square error

$$\text{RMSE}_T = \left( \frac{1}{N_{\text{ref}}} \sum_{p=1}^{N_{\text{ref}}} |T(x_p) - T_{\text{FEM}}(x_p)|^2 \right)^{1/2}, \quad (23)$$

and the relative boundary error

$$\text{RelErr}_{\partial\Omega} = \frac{\left( \int_{\partial\Omega} |\gamma_n \iota + h(\gamma_0 T - T_\infty)|^2 \, ds \right)^{1/2}}{\left( \int_{\partial\Omega} |h(\gamma_0 T - T_\infty)|^2 \, ds \right)^{1/2}}. \quad (24)$$

These metrics provide complementary insights, with  $\text{RMSE}_T$  quantifying global deviation and  $\text{RelErr}_{\partial\Omega}$  measuring relative mismatch in port conditions, while absolute-error heat maps reveal spatial error structure. To establish correlation between local residuals and global errors, we rank blockwise indicators  $\eta_i$  in descending order and verify that the top  $k$  peaks in absolute-error heat maps reside within the corresponding micro-patch set  $\bigcup_{i \in I_k} \omega_i$ , with peak intensities scaling proportionally to  $\eta_i$  up to multiplicative constants. The connection between domain-wide energy density and local residual densities is rigorously established through local two-sided bounds. The Supplementary Information (SI) prove the reliability/effectivity bound (Eq. (S187))

$$c'_1 \eta_i^2 \leq \int_{\omega_i} \langle K \nabla e, \nabla e \rangle dx + \int_{\Gamma_i} h, (\gamma_0 e)^2 ds \leq c'_2 \eta_i^2. \quad (25)$$

To capture boundary-layer geometry at the  $h_i$  scale, the Supplementary Information (SI) defines smoothed density maps (Equations (S195)–(S196) of the Supplementary Information (SI)) and proves the pointwise two-sided control on the shrunken core  $\omega_i^\circ$  (Eq. (S197) of the Supplementary Information (SI))

$$\begin{aligned} E_i(x) := S_i \xi(x) + S_i^\Gamma \zeta(x), \quad \mathcal{R}_i(x) := S_i \langle K^{-1} \mathcal{R}_{\text{twist}}, \mathcal{R}_{\text{twist}} \rangle + S_i (h_i^2 |\mathcal{R}_{\text{div}}|^2) + S_i^\Gamma (h_i |\mathcal{R}_{\text{port}}|^2), \\ c_{\min} E_i(x) \leq \mathcal{R}_i(x) \leq c_{\max} E_i(x) \quad (x \in \omega_i^\circ). \end{aligned} \quad (26)$$

These inequalities collectively quantify the strict alignment of boundary-layer ridges with port-dominant regions, where error ridges align precisely with regions on  $\Gamma_i$  where port terms contribute most significantly. All proofs and constant dependencies, which rely only on  $(k_0, |K|_\infty, h_0, |h|_\infty)$  and shape regularity, are provided in the Sec. IX of the Supplementary Information (SI).

## 4 Quantitative Validation under Geometry–Port Constraints

**Table 1:** The reported learning rate for each method is the manuscript optimum obtained from the unified sweep-and-select protocol. Snapshot comparison across representative learning rates (identical hardware/schedule). We report total wall-clock time, mean time per epoch (s/epoch = total/50,000), and RMSE; values use scientific notation with two decimals.

Model	LR	training time (s)	time/epoch (s)	RMSE
PINN	1e-4	4.50e+04	9.01e-01	1.13e-04
LNN-PINN	7e-4	5.12e+04	1.02e+00	8.23e-05
LSTM-PINN	1e-3	5.97e+03	1.19e-01	8.96e-05
LSTM-LNN-PINN	8e-4	6.36e+03	1.27e-01	3.83e-05

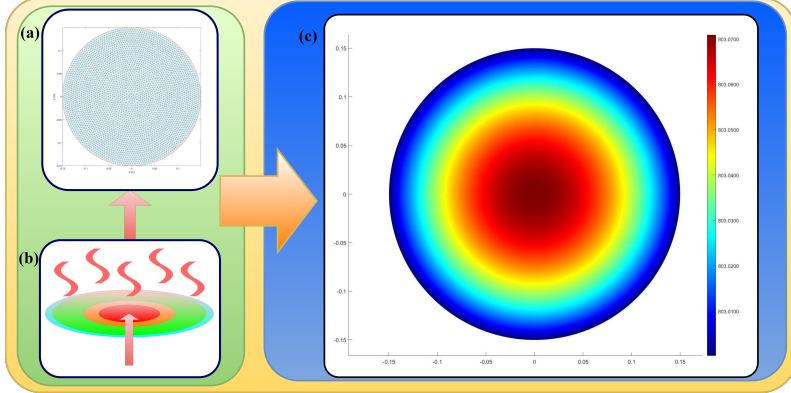


**Fig. 2:** Temperature distribution obtained by numerically simulating the PEB process heat transfer problem using the finite element method on the MATLAB platform. This result serves as a reference benchmark for subsequent computation of RMSE and absolute error distributions for different model predictions. The figure illustrates the spatial distribution of the temperature field within the computational domain, reflecting the effects of finite element discretization and boundary conditions on PEB process thermal behavior. **(a)** We depict the post-exposure bake (PEB) setup: a circular wafer domain  $\Omega$  (radius  $R$ ) with internal heat generation  $Q$  and a convective (Robin) boundary characterized by coefficient  $h$  and ambient temperature  $T_\infty$ ; arrows indicate heat flux and boundary exchange. **(b)** We show the finite-element (FEM) mesh that provides the reference solution, i.e., a conforming triangular tessellation of the circular domain with characteristic element size  $H_{\max}$ , respecting the geometry and boundary ports. **(c)** We present representative outcomes under this setup: the steady-state temperature field  $T(x, y)$  and the absolute-error map  $|T_{\text{model}}(x, y) - T_{\text{FEM}}(x, y)|$ , which we use for visual diagnostics and RMSE evaluation.

We employ a finite-element method (FEM) in MATLAB to generate the reference solution shown in Fig. 2; discretization, solver verification and settings appear in the appendix of our companion paper [70]. Following the unified selection protocol from the Figs. 3 (b), (c) and Figs. 4 (a), (b), we systematically evaluate each backbone architecture by sweeping learning rates from  $10^{-4}$  to  $10^{-3}$  in increments of  $10^{-4}$  under identical conditions, selecting the optimal configuration based on validation RMSE with MAE/MSE and stability as tie-breakers. This benchmarking reveals distinct optimal learning rates for each method: PINN achieves its minimum RMSE of  $1.13 \times 10^{-4}$  at  $1.00 \times 10^{-4}$ , LNN-PINN reaches approximately  $8.23 \times 10^{-5}$  at  $7.00 \times 10^{-4}$ , LSTM-PINN attains about  $8.96 \times 10^{-5}$  at  $1.00 \times 10^{-3}$ , while LSTM-LNN-PINN records the superior performance of  $3.83 \times 10^{-5}$  at  $8.00 \times 10^{-4}$ , demonstrating significant predictive accuracy advantages.

The complete hyperparameter sweep and optimal configurations are documented in the Figs. 3 (b), (c) and Figs. 4 (a), (b) with Tab. 1-5 consolidating the representative settings. The optimal learning rate choices reflect each backbone’s conditioning

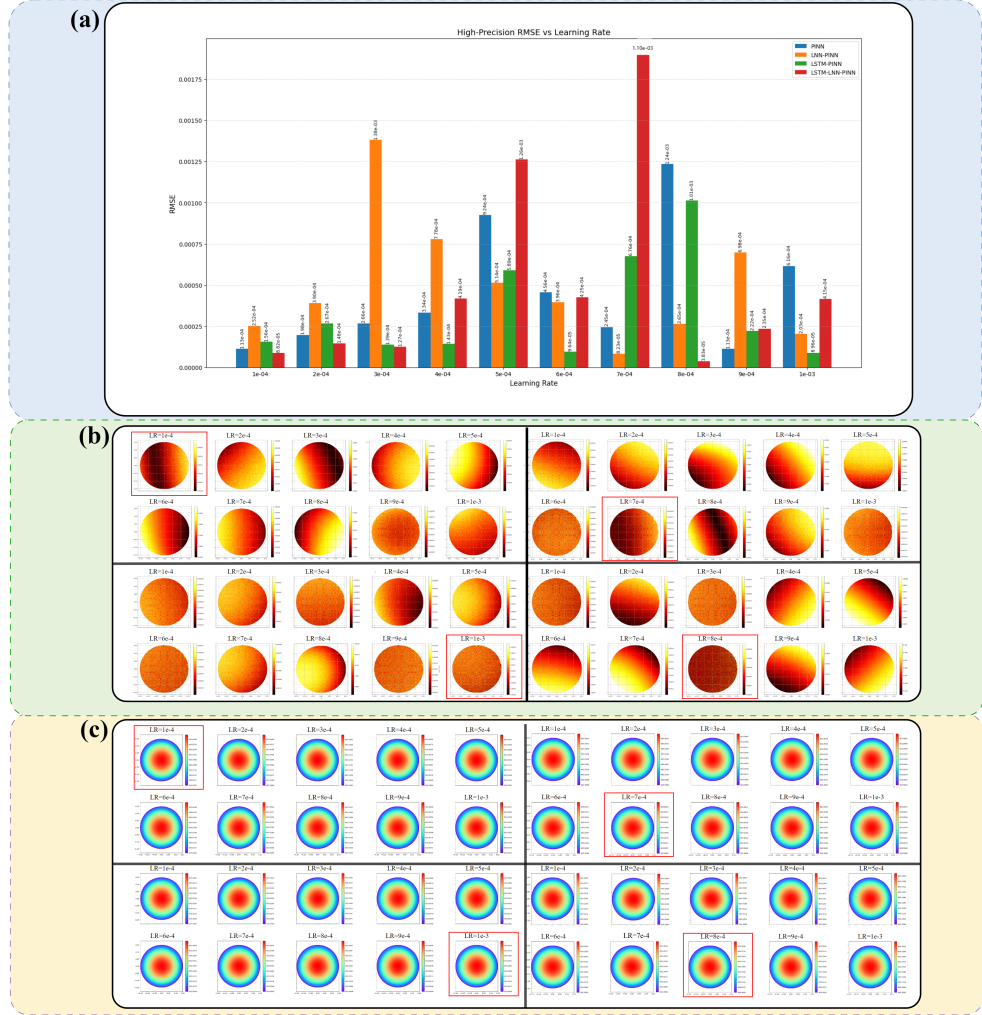


**Fig. 3:** (a) Comparison of Root Mean Square Error (RMSE) for four models—PINN, LNN-PINN, LSTM-PINN, and LSTM-LNN-PINN—under different learning rate settings. The learning rates range from  $1e-4$  to  $1e-3$  in increments of  $1e-4$ . This chart shows how each model’s error responds to different learning rates, reflecting the robustness and sensitivity of the model architectures in solving physical problems. (b) Pointwise absolute error distributions between PINN, LNN-PINN, LSTM-PINN and LSTM-LNN-PINN models predictions and high-precision finite element reference solutions for steady-state heat conduction problems under multiple learning rate settings. Learning rates start from  $1e-4$  and increment by  $1e-4$  up to  $1e-3$ . Each subplot shows the spatial error distribution corresponding to a specific learning rate, providing an intuitive and comparative visualization for evaluating how the LNN-PINN model responds to different optimization intensities in terms of numerical accuracy of the physical field. (c) Temperature field predictions of PINN, LNN-PINN, LSTM-PINN and LSTM-LNN-PINN models, which integrates Liquid Neural Network (LNN) modules, under multiple learning rate settings for steady-state heat conduction problems. Learning rates range from  $1e-4$  to  $1e-3$  with increments of  $1e-4$ . Each subplot corresponds to a specific learning rate, illustrating the model’s simulation performance for temperature distribution across the 2D physical domain. These results provide a visual basis for subsequent error assessment, RMSE analysis, and predictive accuracy comparison, while also reflecting the LNN structure’s ability to capture spatial physical features under different optimization conditions.



**Fig. 4:** (a) Training loss curves of PINN, LNN-PINN, LSTM-PINN and LSTM-LNN-PINN models under multiple learning rate settings plotted in linear coordinates. Learning rates start from  $1e-4$  and increase by  $1e-4$  up to  $1e-3$ , with each curve representing the dynamic evolution of training loss for a specific learning rate. This figure reflects the convergence trends of the model during training and provides a visual basis for understanding the performance of the LSTM-LNN structure within the PINN framework and the effects of learning rate adjustments. (b) Training loss curves of PINN, LNN-PINN, LSTM-PINN and LSTM-LNN-PINN models under different learning rate settings plotted in logarithmic coordinates. Learning rates range from  $1e-4$  to  $1e-3$  with increments of  $1e-4$ . The horizontal axis represents training iterations, and the vertical axis is the logarithmic scale of the loss function, highlighting magnitude changes and subtle fluctuations under different learning rates. This log-scale loss plot provides an important visual reference for evaluating the convergence performance and training stability of the LSTM-LNN-PINN model.

**Table 2:** Learning-rate sweep for the operator-aligned PINN surrogate for PEB heat-flux on silicon wafers: wall-clock training time, per-epoch time, and accuracy metrics (RMSE, MAE, MSE).

<i>LR</i>	training time (s)	time/epoch (s)	RMSE	MAE	MSE
1e-4	4.50e+04	9.01e-01	1.13e-04	9.38e-05	1.27e-08
2e-4	4.50e+04	9.01e-01	1.98e-04	1.87e-04	3.90e-08
3e-4	4.50e+04	9.00e-01	2.66e-04	2.21e-04	7.09e-08
4e-4	4.50e+04	9.01e-01	3.34e-04	3.27e-04	1.11e-07
5e-4	4.50e+04	9.00e-01	9.24e-04	8.84e-04	8.54e-07
6e-4	4.50e+04	9.00e-01	4.56e-04	4.08e-04	2.08e-07
7e-4	4.50e+04	9.00e-01	2.45e-04	2.32e-04	6.02e-08
8e-4	4.50e+04	9.00e-01	1.24e-03	1.21e-03	1.53e-06
9e-4	4.50e+04	9.00e-01	1.13e-04	1.07e-04	1.29e-08
1e-3	4.50e+04	9.00e-01	6.16e-04	6.14e-04	3.80e-07

**Table 3:** Learning-rate sweep for the operator-aligned LNN-PINN surrogate for PEB heat-flux on silicon wafers: wall-clock training time, per-epoch time, and accuracy metrics (RMSE, MAE, MSE).

<i>LR</i>	training time (s)	time/epoch (s)	RMSE	MAE	MSE
1e-4	5.13e+04	1.03e+00	2.52e-04	2.45e-04	6.37e-08
2e-4	5.13e+04	1.03e+00	3.90e-04	3.83e-04	1.52e-07
3e-4	5.13e+04	1.03e+00	1.38e-03	1.34e-03	1.91e-06
4e-4	5.13e+04	1.03e+00	7.78e-04	7.16e-04	6.05e-07
5e-4	5.12e+04	1.02e+00	5.14e-04	5.09e-04	2.65e-07
6e-4	5.08e+03	1.02e-01	3.96e-04	3.94e-04	1.56e-07
7e-4	5.12e+04	1.02e+00	8.23e-05	6.84e-05	6.80e-09
8e-4	5.12e+04	1.02e+00	2.65e-04	2.17e-04	7.00e-08
9e-4	5.12e+04	1.02e+00	6.98e-04	6.93e-04	4.88e-07
1e-3	5.14e+04	1.03e+00	2.03e-04	2.00e-04	4.13e-08

characteristics: PINN performs best at  $1.00 \times 10^{-4}$ , LNN-PINN at  $7.00 \times 10^{-4}$ , LSTM-PINN at  $1.00 \times 10^{-3}$ , and the hybrid LSTM-LNN-PINN at  $8.00 \times 10^{-4}$ . Notably, the gated architectures (LSTM-based) maintain stability at higher learning rates than static baselines, with the hybrid model consistently achieving the lowest RMSE at its optimal rate.

We observe essentially no visible differences among the four predicted temperature fields in the right column of Figs. 3 (c) . For clarity. The absolute-error maps appear in the left column of Figs. 3 (b) , whereas Figs. 4 (a), (b) reports the training-loss curves. All four models provide qualitatively similar fits to the PEB process thermal field at the macroscopic level, but detailed error analysis exposes substantial variations. PINN exhibits edge-concentrated errors reaching  $2.50 \times 10^{-4}$ , indicating limited local stability. LNN-PINN reduces maximum error to  $2.00 \times 10^{-4}$  but maintains significant

**Table 4:** Learning-rate sweep for the operator-aligned LSTM–PINN surrogate for PEB heat-flux on silicon wafers: wall-clock training time, per-epoch time, and accuracy metrics (RMSE, MAE, MSE).

<i>LR</i>	training time (s)	time/epoch (s)	RMSE	MAE	MSE
1e-4	6.21e+03	1.24e-01	1.56e-04	1.52e-04	2.44e-08
2e-4	6.38e+03	1.28e-01	2.67e-04	2.64e-04	7.15e-08
3e-4	5.97e+03	1.19e-01	1.39e-04	1.34e-04	1.94e-08
4e-4	5.90e+03	1.18e-01	1.43e-04	1.28e-04	2.05e-08
5e-4	6.15e+03	1.23e-01	5.89e-04	5.86e-04	3.47e-07
6e-4	6.11e+03	1.22e-01	9.64e-05	9.01e-05	9.30e-09
7e-4	5.99e+03	1.20e-01	6.76e-04	6.74e-04	4.57e-07
8e-4	5.89e+03	1.18e-01	1.01e-03	1.01e-03	1.03e-06
9e-4	6.00e+03	1.20e-01	2.22e-04	2.19e-04	4.92e-08
1e-3	5.97e+03	1.19e-01	8.96e-05	8.26e-05	8.00e-09

**Table 5:** Learning-rate sweep for the operator-aligned LSTM–LNN–PINN surrogate for PEB heat-flux on silicon wafers: wall-clock training time, per-epoch time, and accuracy metrics (RMSE, MAE, MSE).

<i>LR</i>	training time (s)	time/epoch (s)	RMSE	MAE	MSE
1e-4	5.68e+03	1.14e-01	8.82e-05	8.10e-05	7.80e-09
2e-4	5.46e+03	1.09e-01	1.48e-04	1.30e-04	2.18e-08
3e-4	6.10e+03	1.22e-01	1.27e-04	1.22e-04	1.61e-08
4e-4	5.44e+03	1.09e-01	4.19e-04	4.04e-04	1.76e-07
5e-4	6.34e+03	1.27e-01	1.26e-03	1.17e-03	1.60e-06
6e-4	5.44e+03	1.09e-01	4.25e-04	4.05e-04	1.81e-07
7e-4	5.91e+03	1.18e-01	1.90e-03	1.87e-03	3.62e-06
8e-4	6.36e+03	1.27e-01	3.83e-05	3.13e-05	1.50e-09
9e-4	6.27e+03	1.25e-01	2.35e-04	2.08e-04	5.54e-08
1e-3	6.75e+03	1.35e-01	4.15e-04	3.92e-04	1.72e-07

local variations. LSTM-PINN further mitigates error aggregation with a maximum of  $1.60 \times 10^{-4}$ , though uniformity remains suboptimal. In contrast, LSTM-LNN-PINN achieves superior performance with errors below  $1.00 \times 10^{-4}$  uniformly distributed across the domain, demonstrating the architecture’s capacity to suppress systematic bias. This “micro-differentiation under macro similarity” provides crucial insights for method selection in high-precision PEB process simulations.

Comparative analysis of loss convergence in Figs. 4 (a) (b) further elucidates model performance characteristics. While all models exhibit similar overall loss reduction in linear scale, logarithmic scaling reveals fundamental differences in training dynamics. PINN ( $1.00 \times 10^{-4}$ ) converges but suffers from late-stage fluctuations in both PDE and boundary condition losses. LNN-PINN ( $7.00 \times 10^{-4}$ ) displays severe oscillations indicating stability limitations. LSTM-PINN ( $1.00 \times 10^{-3}$ ) maintains stable

PDE loss but continues oscillating in boundary conditions. Only LSTM-LNN-PINN ( $8.00 \times 10^{-4}$ ) demonstrates comprehensive advantages: PDE loss rapidly drops to a minimal plateau ( $\sim 1.00 \times 10^{-6}$ ), boundary condition loss converges synchronously, and overall fluctuations remain substantially smaller than other architectures. These log-scale observations align with RMSE rankings and absolute error distributions, confirming that LSTM-LNN-PINN achieves minimal fluctuations, accelerated convergence, ultra-low loss, and superior stability, fundamentally explaining its leading performance in PEB process thermal field reconstruction.

## 5 Conclusion

This study has developed an operator-aligned LSTM-LNN-PINN for high-fidelity thermal reconstruction in post-exposure bake processes on silicon wafers. The framework maps coordinates to fields to differential operators on a unified computation graph, ensuring strict geometry–port consistency and the simultaneous enforcement of constitutive, balance, and Robin-port relations. Benchmarking against a MATLAB FEM reference confirms the model’s superior accuracy, with the hybrid architecture achieving an RMSE of  $3.83 \times 10^{-5}$  at a learning rate of  $8.00 \times 10^{-4}$  and maintaining domain-wide absolute errors below  $1.00 \times 10^{-4}$ . The robustness of the model is further demonstrated by log-scale residual-energy trajectories that converge rapidly to tight plateaus without late-stage oscillations. Consequently, this work delivers a fast, accurate, and operator-consistent surrogate for PEB heat-flux analysis, with formal proofs for preconditioning equivalence and second-order bounds provided in the Supplementary Information (SI).

## Declaration of competing interest

The authors declared that they have no conflicts of interest to this work.

## Acknowledgment

This work is supported by the developing Project of Science and Technology of Jilin Province (20240402042GH).

## Data availability

All the code for this article is available open access at a Github repository available at <https://github.com/Uderwood-TZ/Operator-Consistent-Physics-Informed-Learning-for-Wafer-Thermal-Reconstruction-in-Lithography.git>.

## References

- [1] Steele, D.A., Coniglio, A., Tang, C., Singh, B., Nip, S., Spanos, C.J.: Characterizing post-exposure bake processing for transient-and steady-state conditions, in the context of critical dimension control. In: *Metrology, Inspection, and Process Control for Microlithography XVI*, vol. 4689, pp. 517–530 (2002). SPIE

- [2] Sturtevant, J.L., Holmes, S.J., Van Kessel, T.G., Hobbs, P.C., Shaw, J.C., Jackson, R.R.: Postexposure bake as a process-control parameter for chemically amplified photoresist. In: Integrated Circuit Metrology, Inspection, and Process Control VII, vol. 1926, pp. 106–114 (1993). SPIE
- [3] Ngo, Y.S., Qu, Y., Tay, A., Lee, T.H.: In-situ critical dimension control during post-exposure bake with spectroscopic ellipsometry. In: Metrology, Inspection, and Process Control for Microlithography XXVI, vol. 8324, pp. 853–863 (2012). SPIE
- [4] Rice, B.J., Cao, H.B., Chandhok, M., Meagley, R.P.: Effects of processing parameters on line-width roughness. In: Advances in Resist Technology and Processing XX, vol. 5039, pp. 384–392 (2003). SPIE
- [5] Leontiou, T., Frixou, A., Charalambides, M., Stiliaris, E., Papanicolas, C.N., Nikolaidou, S., Papadakis, A.: Three-dimensional thermal tomography with physics-informed neural networks. *Tomography* **10**(12), 1930 (2024)
- [6] Liao, S., Xue, T., Jeong, J., Webster, S., Ehmann, K., Cao, J.: Hybrid thermal modeling of additive manufacturing processes using physics-informed neural networks for temperature prediction and parameter identification. *Computational Mechanics* **72**(3), 499–512 (2023)
- [7] Gong, Z., Zhou, W., Zhang, J., Peng, W., Yao, W.: Physics-informed deep reversible regression model for temperature field reconstruction of heat-source systems. Available at SSRN 4123158 (2021)
- [8] Li, R., Lee, E., Luo, T.: Physics-informed neural networks for solving multiscale mode-resolved phonon boltzmann transport equation. *Materials Today Physics* **19**, 100429 (2021)
- [9] Chen, J., Pierce, J., Williams, G., Simpson, T.W., Meisel, N., Prabha Narra, S., McComb, C.: Accelerating thermal simulations in additive manufacturing by training physics-informed neural networks with randomly synthesized data. *Journal of Computing and Information Science in Engineering* **24**(1), 011004 (2024)
- [10] Beck, J.V., Blackwell, B., Clair, C.R.S.: *Inverse Heat Conduction: Ill-posed Problems*. James Beck, ??? (1985)
- [11] Lu, L., Pestourie, R., Yao, W., Wang, Z., Verdugo, F., Johnson, S.G.: Physics-informed neural networks with hard constraints for inverse design. *SIAM Journal on Scientific Computing* **43**(6), 1105–1132 (2021)
- [12] Romano, G., Johnson, S.G.: Inverse design in nanoscale heat transport via interpolating interfacial phonon transmission. *Structural and Multidisciplinary Optimization* **65**(10), 297 (2022)

- [13] Ertürk, H., Daun, K., França, F.H., Hajimirza, S., Howell, J.R.: Inverse methods in thermal radiation analysis and experiment. *ASME Journal of Heat and Mass Transfer* **145**(5), 050801 (2023)
- [14] Venuthurumilli, P.K., Zeng, Z., Xu, X.: Inverse design of near-field transducer for heat-assisted magnetic recording using topology optimization. *IEEE Transactions on Magnetics* **57**(8), 1–6 (2021)
- [15] Nakagawa, M., Noguchi, Y., Matsushima, K., Yamada, T.: Level set-based multiscale topology optimization for a thermal cloak design problem using the homogenization method. *International Journal of Heat and Mass Transfer* **207**, 123964 (2023)
- [16] Oh, H., Jo, G.: Physics-informed neural network for the heat equation under imperfect contact conditions and its error analysis. *AIMS Mathematics* **10**(4), 7920–7940 (2025)
- [17] Tang, H., Melnikov, A., Liu, M., Sfarrà, S., Zhang, H., Mandelis, A.: Physics informed neural networks for solving inverse thermal wave coupled boundary-value problems. *International Journal of Heat and Mass Transfer* **245**, 126985 (2025)
- [18] Murari, K., Sundar, S.: Physics informed neural network for forward and inverse radiation heat transfer in graded-index medium. *arXiv preprint arXiv:2412.14699* (2024)
- [19] Puttock-Brown, M.R., Bindhu, G.K., Ashby, C.E.: A physics-informed neural network for solving the inverse heat transfer problem in gas turbine rotating cavities. *Journal of Turbomachinery* **147**(7), 071010 (2025)
- [20] Xia, Y., Meng, Y.: Physics-informed neural network (pinn) for solving frictional contact temperature and inversely evaluating relevant input parameters. *Lubricants* **12**(2), 62 (2024)
- [21] Kashefi, A., Mukerji, T.: Physics-informed pointnet: A deep learning solver for steady-state incompressible flows and thermal fields on multiple sets of irregular geometries. *Journal of Computational Physics* **468**, 111510 (2022)
- [22] Zheng, J., Li, F., Huang, H.: T-ppinn: Physics-informed neural networks for solving 2d non-fourier heat conduction equations. *International Journal of Heat and Mass Transfer* **235**, 126216 (2024)
- [23] Aygun, A., Karakus, A.: Physics informed neural networks for two dimensional incompressible thermal convection problems. *İş Bilimi ve Tekniği Dergisi* **42**(2), 221–232 (2022)
- [24] Chandan, K., Karthik, K., Nagaraja, K., Prasannakumara, B., Varun Kumar, R.,

Muhammad, T.: Radiative heat transfer analysis of a concave porous fin under the local thermal non-equilibrium condition: application of the clique polynomial method and physics-informed neural networks. *Applied Mathematics and Mechanics* **45**(9), 1613–1632 (2024)

[25] Guo, P., Song, H., Tang, Y., Wang, B., Wang, B.: Application of physics-informed neural network to calculate heat transfer and deuterium diffusion-trapping in tungsten plasma facing materials. *Journal of Intelligent Manufacturing*, 1–27 (2025)

[26] Bonab, S.A., Song, W., Yazdani-Asrami, M.: Physics-informed neural network model for transient thermal analysis of superconductors. *Superconductor Science and Technology* **38**(8), 08–01 (2025)

[27] Zhou, S., Shi, R., Yu, H., Zhang, X., Dai, J., Huang, X., Xu, F.: A physical-informed neural network for improving air-sea turbulent heat flux parameterization. *Journal of Geophysical Research: Atmospheres* **129**(17), 2023–040603 (2024)

[28] Xu, G., Liu, L., Lyu, J., Shao, D., Ma, R., Liu, P., Ao, W.: A physics-informed neural network-enhanced material point method for regression and heat transfer modeling of solid propellant. *International Communications in Heat and Mass Transfer* **167**, 109320 (2025)

[29] Majumdar, R., Jadhav, V., Deodhar, A., Karande, S., Vig, L., Runkana, V.: Hxpin: A hypernetwork-based physics-informed neural network for real-time monitoring of an industrial heat exchanger. *Numerical Heat Transfer, Part B: Fundamentals* **86**(6), 1910–1931 (2025)

[30] Xing, Z., Cheng, H., Cheng, J.: Deep learning method based on physics-informed neural network for 3d anisotropic steady-state heat conduction problems. *Mathematics* **11**(19), 4049 (2023)

[31] Ghaderi, E., Bijarchi, M., Hannani, S.K., Nouri-Borujerdi, A.: Evaluating joule heating influence on heat transfer and entropy generation in mhd channel flow: A parametric study and ill-posed problem solution using pinns. *arXiv preprint arXiv:2406.15810* (2024)

[32] Chandan, K., Srilatha, P., Karthik, K., Raghunandan, M., Nagaraja, K., Gopalakrishnan, E., Kumar, R.V., Gamaoun, F.: Optimized physics-informed neural network for analyzing the radiative-convective thermal performance of an inclined wavy porous fin. *Case Studies in Thermal Engineering* **64**, 105423 (2024)

[33] Jalili, D., Jang, S., Jadidi, M., Giustini, G., Keshmiri, A., Mahmoudi, Y.: Physics-informed neural networks for heat transfer prediction in two-phase flows. *International Journal of Heat and Mass Transfer* **221**, 125089 (2024)

- [34] Xu, J., Wei, H., Bao, H.: Physics-informed neural networks for studying heat transfer in porous media. *International Journal of Heat and Mass Transfer* **217**, 124671 (2023)
- [35] Cai, S., Wang, Z., Wang, S., Perdikaris, P., Karniadakis, G.E.: Physics-informed neural networks for heat transfer problems. *Journal of Heat Transfer* **143**(6), 060801 (2021)
- [36] Zhao, C., Zhang, F., Lou, W., Wang, X., Yang, J.: A comprehensive review of advances in physics-informed neural networks and their applications in complex fluid dynamics. *Physics of Fluids* **36**(10) (2024)
- [37] Bowman, B., Oian, C., Kurz, J., Khan, T., Gil, E., Gamez, N.: Physics-informed neural networks for the heat equation with source term under various boundary conditions. *Algorithms* **16**(9), 428 (2023)
- [38] Bararnia, H., Esmaeilpour, M.: On the application of physics informed neural networks (pinn) to solve boundary layer thermal-fluid problems. *International Communications in Heat and Mass Transfer* **132**, 105890 (2022)
- [39] Uhrich, B., Pfeifer, N., Schäfer, M., Theile, O., Rahm, E.: Physics-informed deep learning to quantify anomalies for real-time fault mitigation in 3d printing. *Applied Intelligence* **54**(6), 4736–4755 (2024)
- [40] Ranjbar, A.M., Pouransari, Z., Siavashi, M.: Improved design of heat sink including porous pin fins with different arrangements: A numerical turbulent flow and heat transfer study. *Applied Thermal Engineering* **198**, 117519 (2021)
- [41] Ali, N., Srivastava, S., Haque, I., Yadav, J., Alam, T., Siddiqui, T.U., Siddiqui, M.I.H., Cuce, E.: Heat dissipation and fluid flow in micro-channel heat sink equipped with semi-elliptical pin-fin structures: A numerical study. *International Communications in Heat and Mass Transfer* **155**, 107492 (2024)
- [42] Zhang, B., Wu, G., Gu, Y., Wang, X., Wang, F.: Multi-domain physics-informed neural network for solving forward and inverse problems of steady-state heat conduction in multilayer media. *Physics of Fluids* **34**(11) (2022)
- [43] Jeon, J., Lee, J., Vinuesa, R., Kim, S.J.: Residual-based physics-informed transfer learning: A hybrid method for accelerating long-term cfd simulations via deep learning. *International Journal of Heat and Mass Transfer* **220**, 124900 (2024)
- [44] Pang, H., Wu, L., Liu, J., Liu, X., Liu, K.: Physics-informed neural network approach for heat generation rate estimation of lithium-ion battery under various driving conditions. *Journal of Energy Chemistry* **78**, 1–12 (2023)
- [45] Guo, H., Zhuang, X., Fu, X., Zhu, Y., Rabczuk, T.: Physics-informed deep learning for three-dimensional transient heat transfer analysis of functionally graded

materials. *Computational Mechanics* **72**(3), 513–524 (2023)

- [46] Kashefi, A., Mukerji, T.: Prediction of fluid flow in porous media by sparse observations and physics-informed pointnet. *Neural Networks* **167**, 80–91 (2023)
- [47] Manavi, S., Becker, T., Fattah, E.: Enhanced surrogate modelling of heat conduction problems using physics-informed neural network framework. *International Communications in Heat and Mass Transfer* **142**, 106662 (2023)
- [48] Shang, Y., Ban, H., Liu, D.: Simultaneous identification of boundary heat flux and thermal conductivity in inverse heat conduction problems using physics-informed neural networks. *Thermal Science and Engineering Progress*, 103905 (2025)
- [49] Peng, J.-Z., Aubry, N., Li, Y.-B., Chen, Z.-H., Mei, M., Hua, Y.: Hcp-pign: Efficient heat conduction prediction by physics-informed graph convolutional neural network. *International Journal of Heat and Fluid Flow* **109**, 109552 (2024)
- [50] Asadzadeh, M.Z., Roppert, K., Raninger, P.: Material data identification in an induction hardening test rig with physics-informed neural networks. *Materials* **16**(14), 5013 (2023)
- [51] Aliakbari, M., Soltany Sadrabadi, M., Vadasz, P., Arzani, A.: Ensemble physics informed neural networks: A framework to improve inverse transport modeling in heterogeneous domains. *Physics of Fluids* **35**(5) (2023)
- [52] Du, Z., Lu, R.: Physics-informed neural networks (pinn) for advanced thermal management in electronics and battery system: A review of recent developments and future prospects (2025)
- [53] Torres, E., Schiefer, J., Niepert, M.: Adaptive physics-informed neural networks: A survey. *arXiv preprint arXiv:2503.18181* (2025)
- [54] Leng, K., Shankar, M., Thiyyagalingam, J.: Zero coordinate shift: Whetted automatic differentiation for physics-informed operator learning. *Journal of Computational Physics* **505**, 112904 (2024)
- [55] Burbulla, S.: Physics-informed neural networks for transformed geometries and manifolds. *arXiv preprint arXiv:2311.15940* (2023)
- [56] Franco, N.R., Manzoni, A., Zunino, P.: Mesh-informed neural networks for operator learning in finite element spaces. *Journal of Scientific Computing* **97**(2), 35 (2023)
- [57] Oldenburg, J., Borowski, F., Öner, A., Schmitz, K.-P., Stiehm, M.: Geometry aware physics informed neural network surrogate for solving navier–stokes equation (gapinn). *Advanced Modeling and Simulation in Engineering Sciences* **9**(1), 8 (2022)

- [58] Gao, H., Sun, L., Wang, J.-X.: Phygeonet: Physics-informed geometry-adaptive convolutional neural networks for solving parameterized steady-state pdes on irregular domain. *Journal of Computational Physics* **428**, 110079 (2021)
- [59] Gao, W., Xu, R., Deng, Y., Liu, Y.: Discretization-invariance? on the discretization mismatch errors in neural operators. In: The Thirteenth International Conference on Learning Representations (2025)
- [60] Gokhale, G., Claessens, B., Develder, C.: Physics informed neural networks for control oriented thermal modeling of buildings. *Applied Energy* **314**, 118852 (2022)
- [61] Merdasi, A., Ebrahimi, S., Yang, X., Kunz, R.: Physics informed neural network application on mixing and heat transfer in combined electroosmotic-pressure driven flow. *Chemical Engineering and Processing-Process Intensification* **193**, 109540 (2023)
- [62] Farea, A., Yli-Harja, O., Emmert-Streib, F.: Understanding physics-informed neural networks: Techniques, applications, trends, and challenges. *AI* **5**(3), 1534–1557 (2024)
- [63] Ren, Z., Zhou, S., Liu, D., Liu, Q.: Physics-informed neural networks: A review of methodological evolution, theoretical foundations, and interdisciplinary frontiers toward next-generation scientific computing. *Applied Sciences* **15**(14), 8092 (2025)
- [64] Ganga, S., Uddin, Z.: Exploring physics-informed neural networks: From fundamentals to applications in complex systems. *arXiv preprint arXiv:2410.00422* (2024)
- [65] Jiao, R., Cai, S., Braun, J.: Solving crustal heat transfer for thermochronology using physics-informed neural networks. *Geochronology* **6**(2), 227–245 (2024)
- [66] Laubscher, R.: Simulation of multi-species flow and heat transfer using physics-informed neural networks. *Physics of Fluids* **33**(8) (2021)
- [67] Zhao, Z., Wang, Y., Zhang, W., Ba, Z., Sun, L.: Physics-informed neural networks in heat transfer-dominated multiphysics systems: A comprehensive review. *Engineering Applications of Artificial Intelligence* **157**, 111098 (2025)
- [68] Cuomo, S., Di Cola, V.S., Giampaolo, F., Rozza, G., Raissi, M., Piccialli, F.: Scientific machine learning through physics-informed neural networks: Where we are and what's next. *Journal of Scientific Computing* **92**(3), 88 (2022)
- [69] Klapa Antonion, X.W., Raissi, M., Joshie, L.: Machine learning through physics-informed neural networks: Progress and challenges. *Academic Journal of Science and Technology* **9**(1), 2024 (2024)

[70] Tao, Z., Wang, H., Liu, F.: Lnn-pinn: A unified physics-only training framework with liquid residual blocks. arXiv preprint arXiv:2508.08935 (2025)